AGU PUBLICATIONS

JGR

Journal of Geophysical Research: Solid Earth

RESEARCH ARTICLE

10.1002/2014JB011253

Key Points:
- MTZ discontinuities are imaged using over 310,000 receiver functions
- The MTZ thickness corresponds well with subducted slabs and lithospheric drips
- The MTZ beneath Yellowstone and Raton is normal but thinner beneath Bermuda

Supporting Information:
- Readme
- Table S1
- Figure S1

Correspondence to:
S. S. Gao,
sgao@mst.edu

Citation:
Gao, S. S., and K. H. Liu (2014), Mantle transition zone discontinuities beneath the contiguous United States, *J. Geophys. Res. Solid Earth*, *119*, 6452–6468, doi:10.1002/2014JB011253.

Received 6 MAY 2014
Accepted 25 JUL 2014
Accepted article online 1 AUG 2014
Published online 14 AUG 2014

Mantle transition zone discontinuities beneath the contiguous United States

Stephen S. Gao[1] and Kelly H. Liu[1]

[1]Geology and Geophysics Program, Missouri University of Science and Technology, Rolla, Missouri, USA

Abstract Using over 310,000 high-quality radial receiver functions recorded by the USArray and other seismic stations in the contiguous United States, the depths of the 410 km and 660 km discontinuities (d410 and d660) are mapped in over 1,000 consecutive overlapping circles with a radius of 1°. The average mantle transition zone (MTZ) thickness for both the western and central/eastern U.S. is within 3 km from the global average of 250 km, suggesting an overall normal MTZ temperature beneath both areas. The Pacific Coast Ranges and the southern Basin and Range Province are underlain by a depressed d410, indicating higher-than-normal temperature in the upper MTZ. The proposed Yellowstone and Raton hot spots are not associated with clear undulations of the MTZ discontinuities, but d410 beneath another proposed hot spot, Bermuda, is depressed significantly and d660 has a normal depth. Low-temperature regions are found in the upper MTZ associated with the subducted Juan de Fuca slab beneath the northern Rocky Mountains and in two circular areas beneath the northern Basin and Range Province and the southern Colorado Plateau. Part of the Great Plains is characterized by a depressed d660. This observation, when combined with results from seismic tomography, suggests the existence of a cold region in the lower MTZ, probably associated with subducted Farallon slab segments.

1. Introduction

Determining the depth extent of major tectonic features observed on or near the Earth's surface, such as orogenic zones, subducting slabs, and mantle plumes, is the key to address a number of first-order problems in global tectonics related to the structure, evolution, and dynamics of the Earth's interior. Seismic tomography is the main tool for exploring the Earth's internal structures. Unfortunately, due to the diminishing resolving power with increasing depth of all the seismic tomographic techniques and the limited lateral resolution, the depth extent for most of the aforementioned features remains controversial. The topography of the 410 km (d410) and 660 km (d660) discontinuities, which represent olivine to wadsleyite and ringwoodite to perovskite phase transitions at the top and bottom of the mantle transition zone (MTZ), respectively [*Ringwood*, 1975], provides independent constraints on the depth extent of the tectonic features [*Shearer*, 1991]. The depth of d410 (d660) in both the IASP91 [*Kennett and Engdahl*, 1991] and AK135 [*Kennett et al.*, 1995] Earth models is 410 (660) km but is 400 (670) km in the PREM model [*Dziewonski and Anderson*, 1981]. The study of *Flanagan and Shearer* [1998] gave a global average of 418 km for the depth of d410, and 660 km for d660, while *Gu et al.* [1998] suggested 411 and 652 km, respectively. Following *Cao and Levander* [2010], we use the IASP91 and AK135 MTZ discontinuity depths of 410 and 660 km as the reference depths.

Under normal temperature and anhydrous conditions, the Clapeyron slope of the phase transition across d410 is positive, with reported values ranging from +1.5 to +3.0 MPa/K. This suggests that d410 uplifts in areas with reduced temperature such as that associated with subducted slabs and depresses under high-temperature conditions which are expected when a mantle plume traverses d410. In contrast, d660 behaves in the opposite sense because the ringwoodite-perovskite phase transition has a negative Clapeyron slope. Reported values (ranging from −0.4 to −4.0 MPa/K) of the slope are not consistent among previous studies, making it difficult to accurately estimate the magnitude of temperature anomalies associated with the undulation of d660 [*Bina and Helffrich*, 1994; *Katsura et al.*, 2003; *Fei et al.*, 2004; *Litasov et al.*, 2005]. Temperature estimates presented below use a slope of 2.9 MPa/K for d410 [*Bina and Helffrich*, 1994] and −1.3 MPa/K for d660 [*Fei et al.*, 2004]. When the temperature in the lower MTZ is significantly higher-than-normal (≥~1750°C), d660 represents the transition from majorite to perovskite, which has a Clapeyron slope of about +1.0 MPa/K [*Hirose*, 2002; *Deuss et al.*, 2006]. The presence of water has the same effects as low temperature on the topography of the MTZ discontinuities [*Smyth*, 1987; *Smyth and Frost*,

2002; *Litasov et al.*, 2005]. For instance, water is an alternative explanation for very large (about 1000°K) temperature anomalies associated with the observed 35 km depression of d660 beneath the northern Colorado Plateau [*Cao and Levander*, 2010].

The contiguous United States and adjacent areas are ideal to investigate the depth extent of some of the world's most prominent tectonic features using the topography of the MTZ discontinuities for a number of reasons. First, the area is composed of the tectonically active western United States (WUS) and the relatively inactive central and eastern United States (CEUS). Determining whether the sharp contrasts in surface topography and tectonic activity extend to the MTZ or lower mantle provides important constraints on such first-order models as top-down or bottom-up tectonics [*Anderson*, 2001]. Second, a number of mantle plumes have been proposed, including the Yellowstone, Raton, and Bermuda [*Morgan*, 1983; *Morgan and Phipps Morgan*, 2007] (Figure 1). Whether the plumes originate from the upper or lower mantle or the mantle transition zone is still a heatedly debated issue [*Leeman et al.*, 2009; *Smith et al.*, 2009; *Fouch*, 2012], and is essential for global mantle circulation models. Third, the NW part of the study area is underlain by the subducted Juan de Fuca plate, and thus is an ideal locale to study the interaction between the MTZ discontinuities and the presumably cold slab. Fourth, it has been proposed that at least part of the approximately 5000 km long Farallon slab subducted over the past 150 million years [*Torsvik et al.*, 2010] is still in the MTZ and lower mantle beneath the CEUS [*Sigloch*, 2011; *Pavlis et al.*, 2012; *Porritt et al.*, 2013]. Testing this hypothesis and addressing the question of whether the slab still possesses observable temperature anomalies are important to understand mantle properties and dynamics. Fifth, some recent high-resolution seismic tomography studies for the contiguous United States [e.g., *Porritt et al.*, 2013; *Burdick et al.*, 2014] make it possible for performing corrections of the observed MTZ discontinuity depths. Finally, data from the USArray, which is near its commencement stage for the contiguous United States, provide an excellent opportunity for a high-resolution continental-scale study of the MTZ discontinuities.

2. Data and Methods

2.1. Data

We requested all the broadband seismic data archived at the Incorporated Research Institutions for Seismology (IRIS) Data Management Center recorded by all the stations located in the area of 25°N to 50°N, and −125°E to −65°E. The seismograms were recorded during a 25+ year period from early 1988 to late 2013, with vastly different lengths of recording among the stations. The epicentral distance of the events ranges from 30° to 180°. To balance the quantity and quality of the seismic data to be requested, cutoff magnitudes (M_c) that are dependent on the epicentral distances and focal depths were used. M_c is defined as $M_c = 5.2 + (\Delta - 30.0)/(180.0 - 30.0) - D/700.0$, where Δ is the epicentral distance in degree and D is the focal depth in kilometer [*Liu and Gao*, 2010].

The requested seismograms were windowed 20 s before and 260 s after the first arrival and were filtered in the frequency band of 0.02–0.2 Hz. Filtered seismograms with a signal-to-noise ratio (S/N) of 4.0 or greater on the vertical component were converted into radial receiver functions (RFs) using the procedure of *Ammon* [1991]. The S/N is calculated using $S_1 = \max|A_s|/|\bar{A_n}|$, where $\max|A_s|$ is the maximum absolute value on the seismogram in the time window of 8 s before and 12 s after the predicted IASP91 arrival time for the first P wave, and $|\bar{A_n}|$ is the mean absolute value on the seismogram in the time window of 10–20 s before the predicted arrival time. To minimize the degenerating effect of the strong PP arrivals on the resulting RFs, the seismograms were preprocessed using an exponential weighting function with a half width of 30 s centered at the PP theoretical arrival time [see *Gao and Liu*, 2013 for details]. The direct compressional wave arrival is at 10 s from the beginning of the RFs, which have a total length of 260 s.

We use the following S/N based procedures to select high-quality RFs:

1. To reject RFs with strong noise before the P wave arrival, an RF is rejected if $S_2 < 1.5$, where S_2 is defined as $\max|A_s|/\max|A_n|$, in which $\max|A_s|$ is the maximum absolute value on the RF in the time window of 1 s before and 1 s after the P wave arrival, and $\max|A_n|$ is the maximum absolute value in the time window 1–10 s before the P wave arrival.
2. To reject RFs with abnormally large arrivals in the P wave coda, a RF is not used if $S_3 < 1.2$ where S_3 has the same form as S_2 but $\max|A_n|$ is the maximum absolute value in the time window from 7 s after the direct P wave to the end of the RF. The value of 7 s is used to exclude the P-to-S converted phase from the Moho.

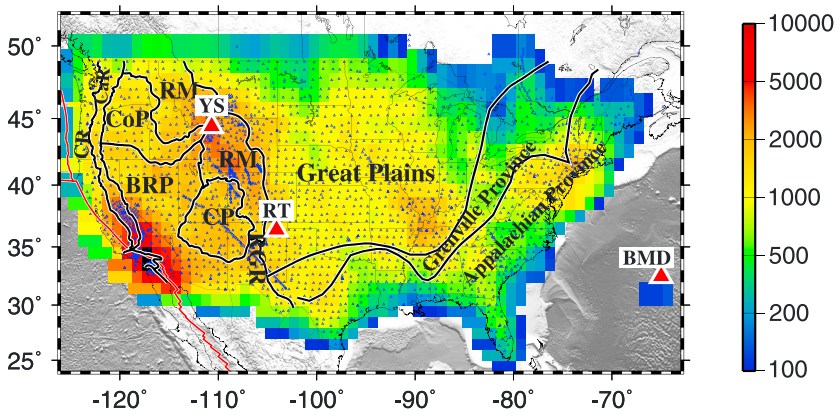

Figure 1. Number of RFs in radius=1° circles and broadband seismic stations (small black triangles) used in the study. The large red triangles represent possible hot spots (YS: Yellowstone, RT: Raton, and BMD: Bermuda), and the thick black lines outline major tectonic provinces [*Hoffman*, 1988; *Lowry et al.*, 2000] (CR: Coast Ranges, CaR: Cascade Range-Sierra Nevada, CoP: Columbia Plateau, BRP: Basin and Range Province, RM: Rocky Mountains, CP: Colorado Plateau, and RGR: Rio Grande Rift).

A total of 316,246 high-quality RFs recorded by 2,848 stations (Figure 1) from 6,315 events (Figure 2) were selected for the study. The number of RFs from stations west of 102°W is 197,626. In comparison, for approximately the same area, the number of RFs is 9,600, 89,536, and 67,000 used by *Cao and Levander* [2010], *Pavlis* [2011], and *Tauzin et al.* [2013], respectively. For the area west of 88°W, the number of RFs used by *Schmandt et al.* [2012] is about 111,820; and for the same area, the number of RFs used in this study is 266,474.

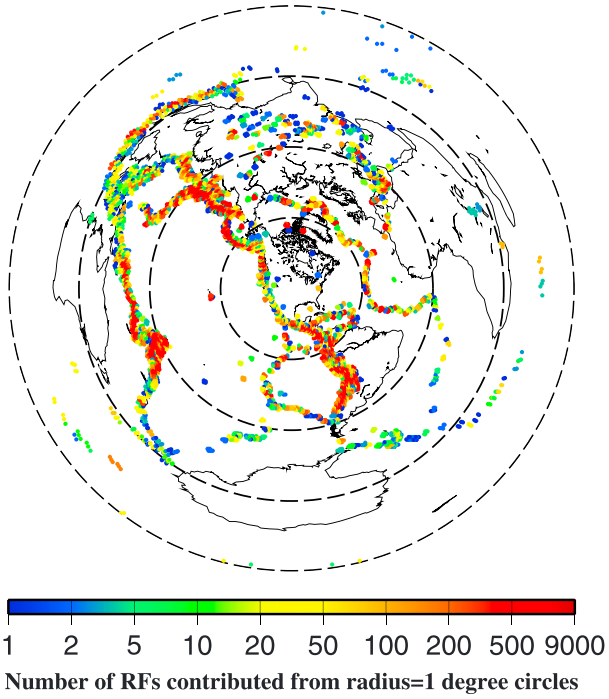

Figure 2. Spatial distribution of earthquake source areas. Each dot represents a radius = 1° circular area. The distance between neighboring circles is 1°. The color of the dot represents the number of used receiver functions originated from earthquakes in the circle. Note the nonlinear nature of the scale bar. The radius of the concentric dashed circles increases at a step of 45°.

2.2. Moveout Correction and Stacking

The procedure for moveout correcting and stacking of *P*-to-*S* converted phase (Pds) arrivals can be found in *Gao and Liu* [2013] and is described briefly here. The procedure is similar to the common-conversion-point (CCP) method [*Dueker and Sheehan*, 1997] but uses the nonplane wavefront assumption. It first computes the coordinates of the ray-piercing point for each of the RFs at the depth of 530 km (which is approximately at the middle of the MTZ), and then groups the RFs based on the location of the piercing points into circles with a radius of 1°, which is approximately the radius of the first Fresnel zone at the MTZ depth range. The distance between the center of neighboring circles is also 1°, and consequently, there is an overlap between neighboring circles.

The RFs in a given circle are then moveout corrected and stacked to form a depth series using

$$S(d) = \frac{1}{N}\sum_{i=1}^{N} S_i(t_i), \qquad (1)$$

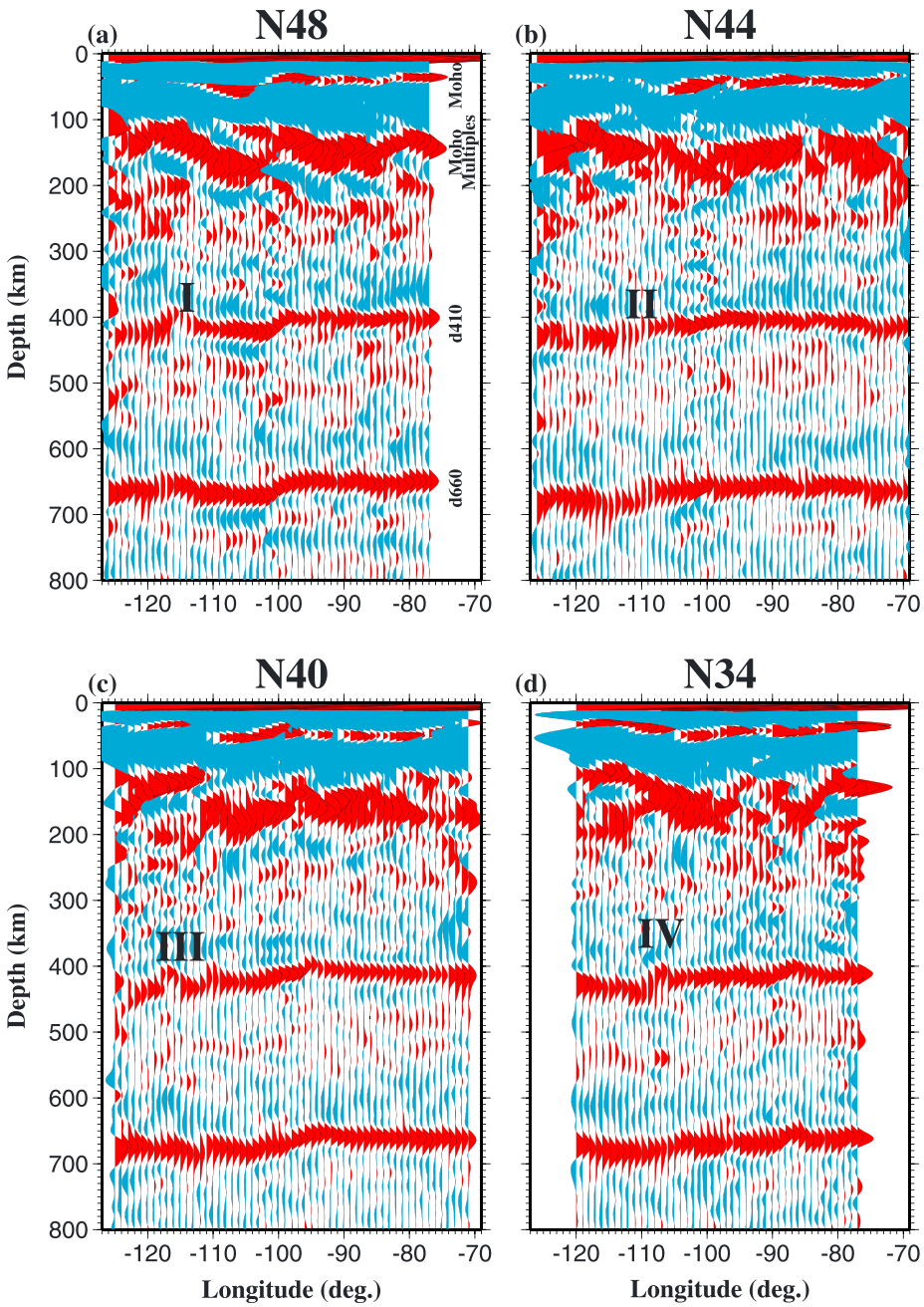

Figure 3. Example plots of depth series along four latitudinal lines. Marked features are as follows: I: Juan de Fuca slab; II: Yellowstone; III: proposed lithospheric drip beneath the northern Basin and Range Province [*West et al.*, 2009]; IV: d410 uplift beneath the southern Colorado Plateau. Similar plots for all the 26 latitudinal lines can be found in Figure S1 in the supporting information.

where $S(d)$ is the stacking amplitude for a candidate discontinuity at depth d, N is the number of RFs in the circle, t_i is the nonplane wave Pds moveout time of the ith receiver function at depth d computed using the IASP91 standard Earth model, and $S_i(t_i)$ is the amplitude of the ith receiver function at time t_i. To ensure reliability, a circle is not used if N is less than 100. In the study area, the number of RFs per circle ranges from 100 to 10,930 and is the highest in Southern and central California, in the vicinity of the Yellowstone Caldera, and in the New Madrid Seismic Zone (NMSZ) due to the numerous permanent and portable seismic network stations (Figure 1) in those areas. The edges of the study area are sampled by low numbers of RFs, and thus the results are not as reliable as those in the interior.

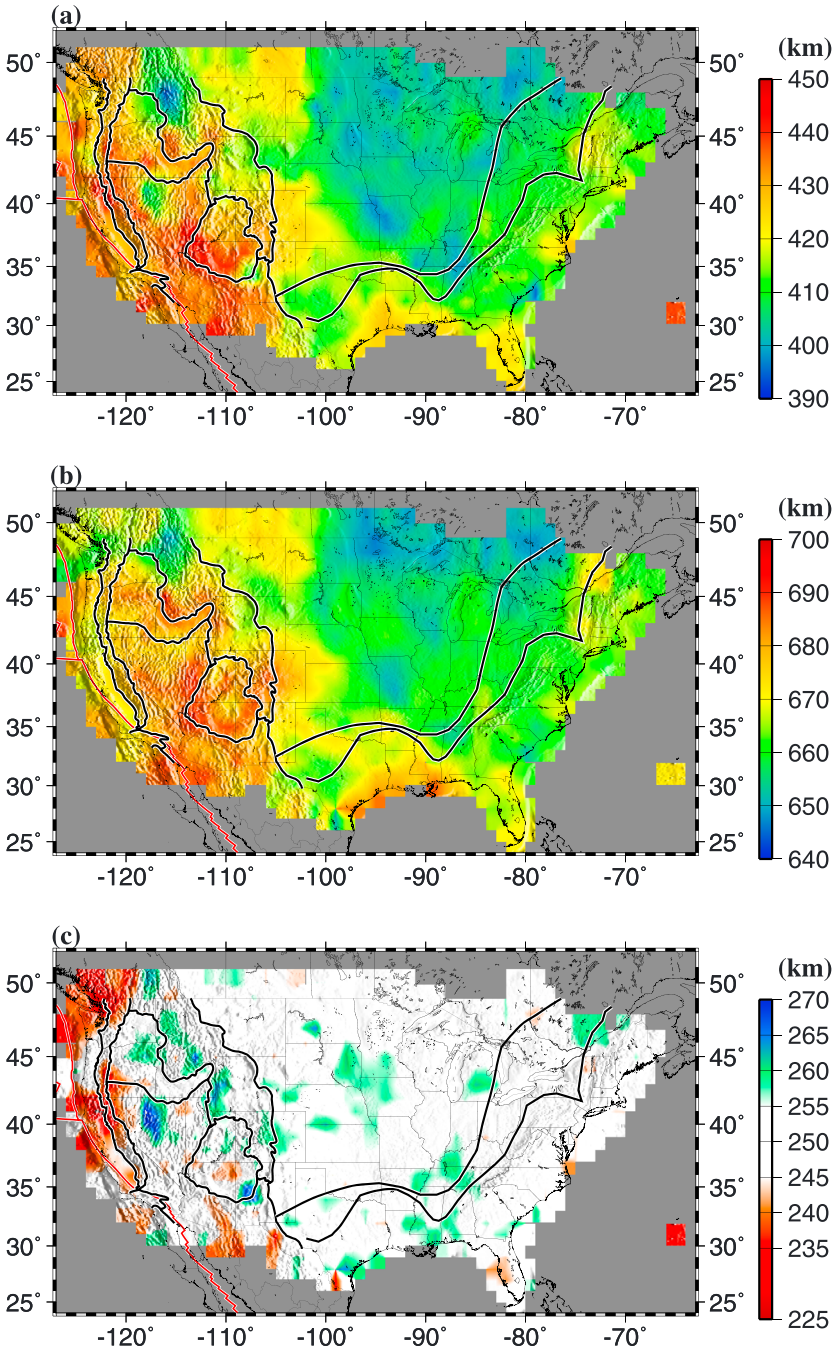

Figure 4. Results of RF stacking based on the IASP91 Earth model: (a) d410 depths, (b) d660 depths, and (c) MTZ thickness. Note that in Figure 4c, the colored areas have a MTZ thickness that differs from the IASP91 value of 250 km by 5 km or greater.

Figure 3 shows resulting depth series along four representative latitudinal cross sections. The depths to d410 and d660 were determined manually from the depth series, and the mean and standard deviation (SD) of the depths were obtained from 10 bootstrap resampling iterations using the same procedure described in *Liu et al.* [2003]. The large number of RFs per circle for most of the study area leads to well-defined d410 and d660 arrivals (Figure 3), resulting in reliably determined mean and SD values for the vast majority of the circles.

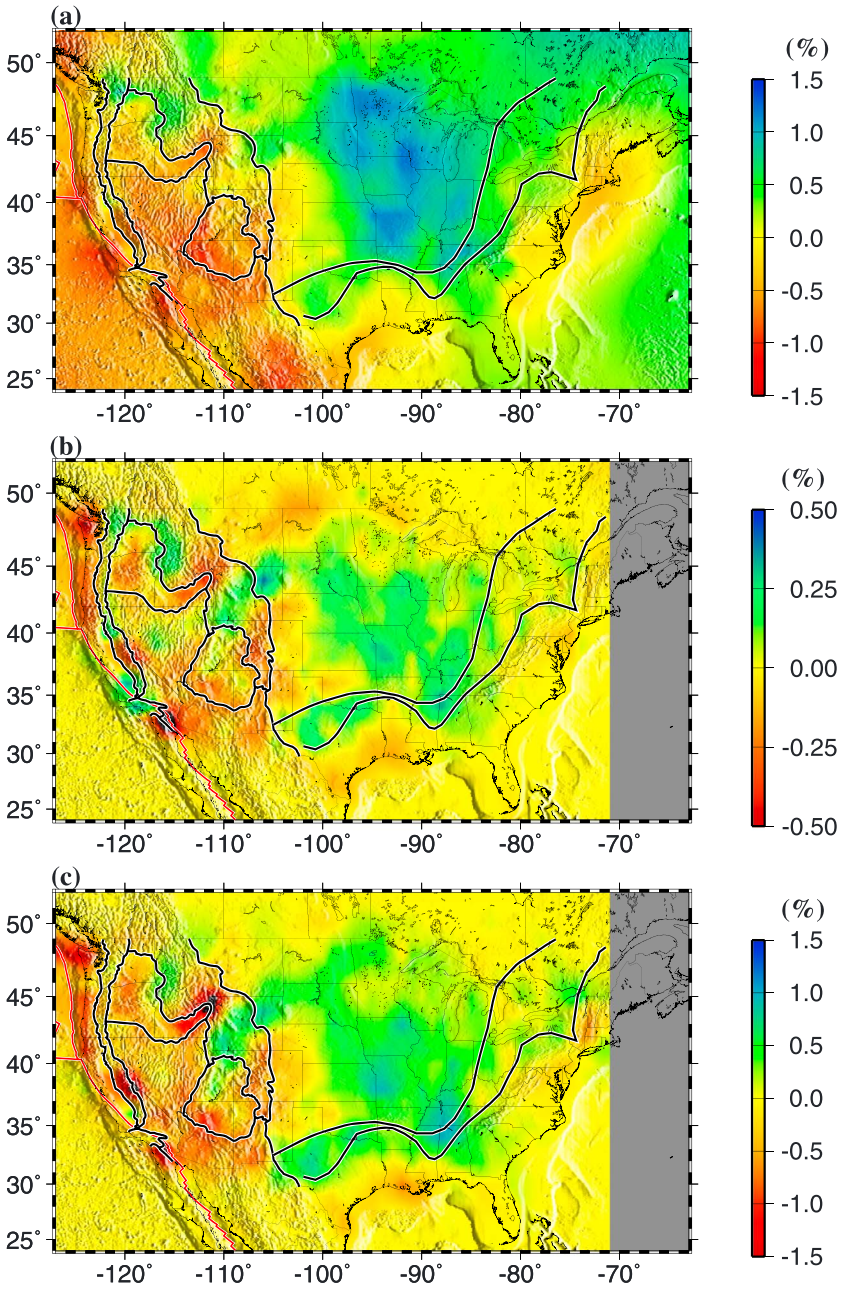

Figure 5. Average upper mantle velocity anomalies. (a) V_P from *Burdick et al.* [2014]. (b) V_P from *Porritt et al.* [2013]. (c) V_S from *Porritt et al.* [2013]. Note the different color scales in Figures 5a and 5b.

Like all the previous CCP-based RF stacking studies, this study assumes flat discontinuities in the $R = 1°$ circles. While short-wavelength random undulations of the topography of the discontinuities in the circle can be averaged out, systematic tilting of the discontinuities has several effects, including reduction in the stacking amplitude and broadening of the Pds arrivals due to incoherent stacking, and multiple arrivals if there are sudden changes in the depth of the discontinuities within the circle. Rapid lateral variations in seismic velocities above the discontinuities have similar effects. For these reasons, the approach is not ideal to image nonhorizontal subducted slabs, which can be better imaged by other techniques such as 3-D prestack migration [*Pavlis*, 2011; *Liu and Pavlis*, 2013]. On the other hand, the CCP stacking approach used in this study produces sharper images for horizontal or nearly horizontal discontinuities, which are the targets of this study, than pre-stack migration [*Pavlis*, 2011]. Fortunately, for the vast majority of the study area,

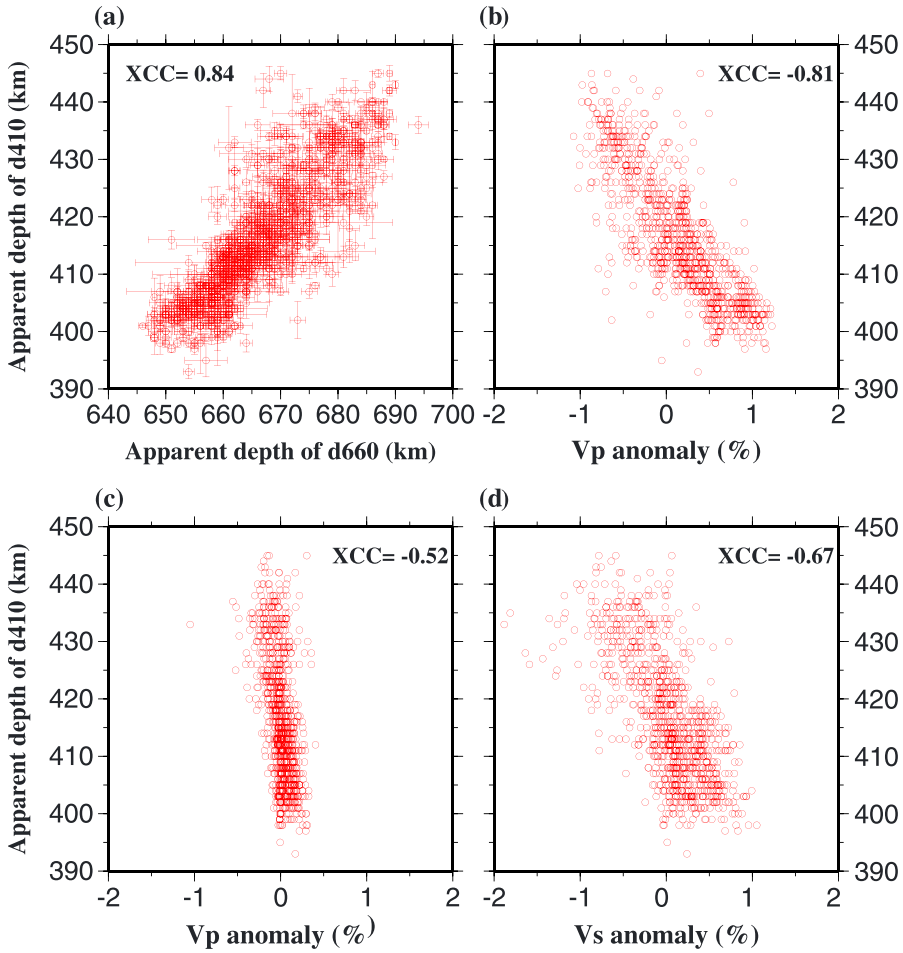

Figure 6. (a) Apparent d410 depths plotted against apparent depths of d660. (b) Apparent d410 depths versus average *P* wave velocity anomalies in the 0–406 km depth range in the MITP13 model. (c) Same as Figure 6b but for V_P anomalies from *Porritt et al.* [2013]. (d) Same as Figure 6c but for V_S anomalies.

the discontinuities are flat enough for the approach to work properly, as evidenced by the sharp arrivals associated with d410 and d660 (Figure S1).

2.3. Velocity Correction

Because the RFs were converted into depth series (Figure 3) by using the 1-D IASP91 standard Earth model (equation (1)), the resulting discontinuity depths are apparent rather than true depths. In order to convert the apparent depths into true depths, accurately determined *P* and *S* wave velocity models are required for the layers above the discontinuities. As proposed in *Gao and Liu* [2013], for a given layer with an apparent thickness of H_A, the true thickness (H_T) can be calculated using

$$H_T = \frac{(V_{s0} + \delta V_s) \times (V_{p0} + \delta V_p)}{V_{p0} + \delta V_p - V_{s0} - \delta V_s} \times \frac{V_{p0} - V_{s0}}{V_{p0} \times V_{s0}} H_A, \tag{2}$$

where V_{p0} and V_{s0} are the mean *P* and *S* wave velocities in the layer in the standard Earth model, and δV_p and δV_s are the absolute *P* and *S* wave velocity anomalies. To be consistent with the 1° spatial interval between the circles, we resample the velocity models into 1° grids horizontally with a 10 km vertical interval.

3. Results

A total of 1055 circles have either clearly observable d410 or d660 arrivals, among which 1043 of them have both. Figure S1 shows all the 1055 depth series plotted along the 26 latitudinal lines (25°N–50°N with an

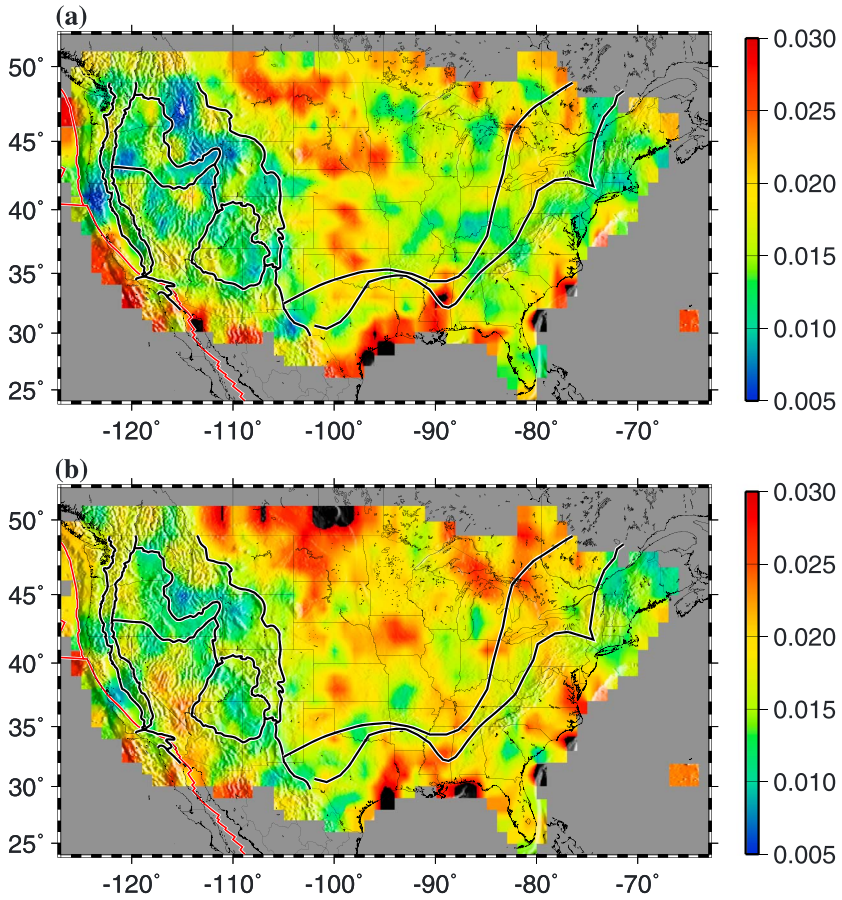

Figure 7. Stacking amplitude (relative to that of the direct *P* wave) for (a) d410 and (b) d660.

increment of 1°). In the following we divide the study area into the WUS and CEUS by the 102°W longitudinal line, which is approximately the eastern extreme of the western U.S. orogenic zone in most of the study area, and is also the boundary between two areas with contrasting apparent MTZ discontinuity depths (Figure 4).

3.1. Apparent d410 and d660 Depths

The resulting apparent depths (i.e., depths before correction using 3-D velocity models) of d410 and d660 show systematic spatial variations (Figure 4 and Table S1). For the entire study area, the average depth is 416±11 km for d410 and 667±10 km for d660. The MTZ thickness is 250±6 km. These values are 425±9, 674±8, and 249±7 km for the WUS, and 410±7, 661±7, and 251±4 km for the CEUS. The depths for the WUS are almost identical to those reported by *Tauzin et al.* [2013] who measured MTZ discontinuities using the IASP91 model for the western U.S. (but excluding central and Southern California) and obtained the values of 424±10 and 676±9 km. They are also consistent with the results of *Cao and Levander* [2010] (425 and 678 km, respectively, for the area west of 108°W). However, we do not observe an ~35 km depression of d660 beneath the northern Colorado Plateau (approximately centered at 111°W and 39°N), although there is a broadening of d660 at this location (Figure S1l). Such a large depression and the associated large temperature reduction of about 1000°K (when a Clapeyron slope of −0.4 MPa/K is used) was proposed as the main evidence for the presence of water in the lower MTZ [*Cao and Levander*, 2010].

In spite of the large difference in the apparent depths between the WUS and CEUS, the two areas have very similar apparent MTZ thickness, suggesting that the observed spatial variations of the apparent depths are mostly caused by lateral velocity heterogeneities above d410. This conclusion is supported by (1) the overall parallelism between the arrivals of d410 and d660 (Figures 3 and S1), (2) the similarity in the spatial pattern between the apparent depths (Figure 4) and the mean upper mantle velocity anomalies (Figure 5), (3) large positive cross-correlation coefficient (XCC) of 0.84 between the apparent depths of d410 and

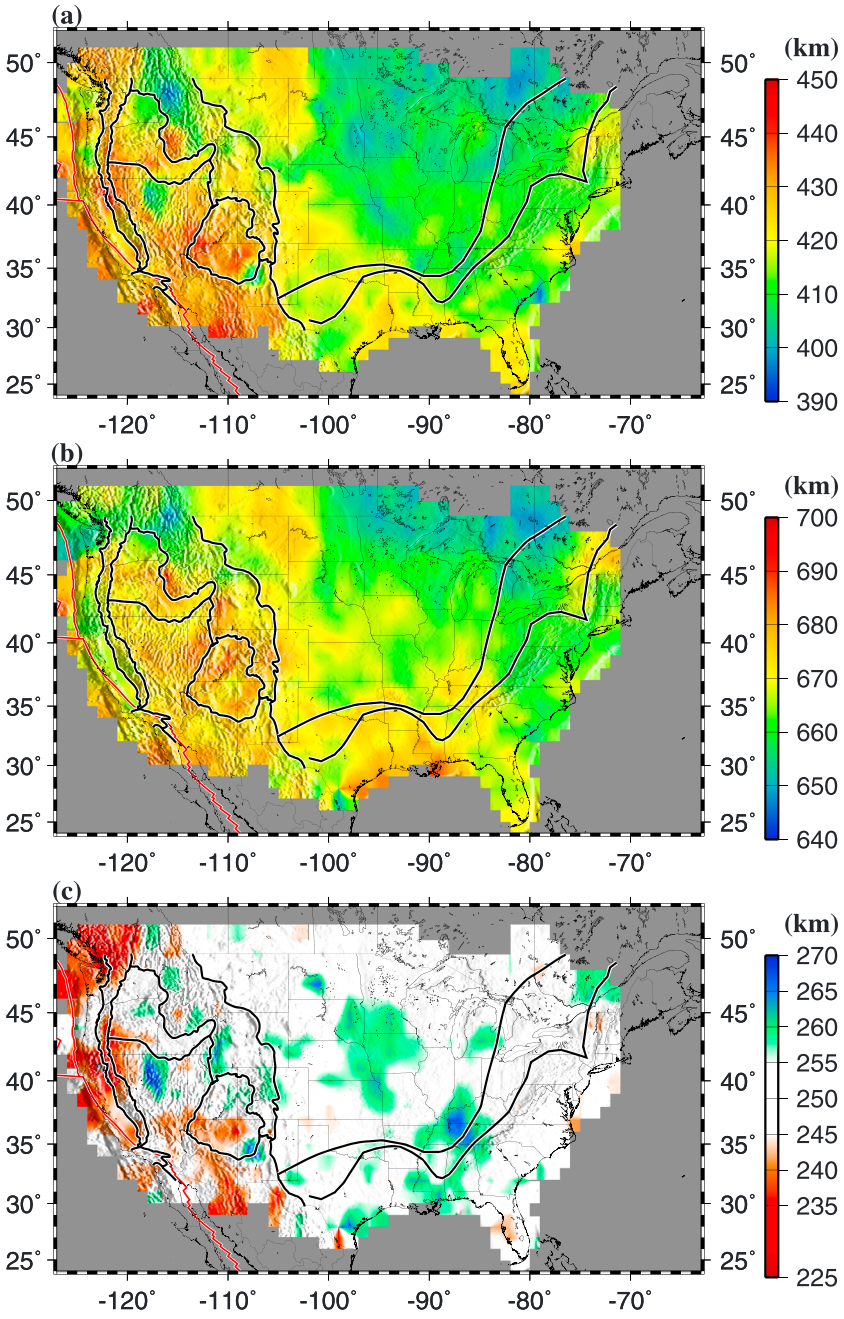

Figure 8. Same as Figure 4 but after corrections using the *P* and *S* wave velocity models of *Porritt et al.* [2013].

d660 (Figure 6a), and (4) the large negative XCCs between the apparent depths of d410 and the velocity anomalies (Figures 6b–6d).

The apparent d410 and d660 depths beneath the CEUS (410 and 661 km, respectively) are almost identical with those in the IASP91 Earth model, suggesting normal mean velocities in the upper mantle when averaged over the whole area. In contrast, the greater-than-normal depths observed in the WUS (425 and 674 km, respectively) indicate slower upper mantle velocities. These observations are consistent with the mean upper mantle velocity anomalies from seismic tomographic inversions (Figure 5).

3.2. Stacking Amplitudes of the Pds Phases

The stacking amplitudes (relative to that of the direct *P* wave) of d410 and d660 (Figure 7) show systematic spatial variations and are spatially correlated with the mean upper mantle velocity anomalies (Figure 5).

In general, in the WUS, where low seismic velocities are found, the amplitudes for both d410 and d660 are smaller than those in the CEUS. One of the possible causes of the difference in stacking amplitudes between the two areas is the difference in the seismic attenuation factor. A more attenuating upper mantle beneath the WUS can lead to a stronger reduction in the amplitude of the *P*-to-*S* converted phases [*Liu*, 2003]. Other possible causes include significant undulations of the discontinuities within a circle, lateral variations of seismic velocities above the discontinuities, variations in the sharpness of the discontinuities, and amplifying effects of near-surface sedimentary layers which might be responsible for the large amplitudes observed along the coast of the Gulf of Mexico.

3.3. Velocity-Corrected Depths

In order to obtain the true depths of the MTZ discontinuities using equation (2) above, reliably determined *P* and *S* wave velocity models with similar spatial and depth resolutions are required. Among the many recent models for the study area, in this study we use the *P* and *S* wave models of *Porritt et al.* [2013], which cover the area west of 72°W, and the *P* wave model of *Burdick et al.* [2014], which covers the entire study area, for velocity corrections. Both are high-resolution body wave velocity models that used data from USArray. In the following the former is called DNA13 (Dynamic North America, 2013), and the latter is referred to as MITP13 (Figure 5).

3.3.1. Correction Using DNA13

DNA13 covers the area of 25°N to 52°N and 126°W to 72°W with a 0.5° node spacing and a 10 km vertical spacing. The shear wave velocity model used for making depth corrections in this study is DNA13-Sv. Figure 8 shows the corrected depths using DNA13, based on the procedure described in section 2.3. The mean value of the corrected depths for the entire area is 417±9 km and 667±8 km for d410 and d660, respectively, and the mean MTZ thickness is 251±7 km. For the WUS, these values are 423±8, 671±7, and 248±8 km; and for the CEUS, they are 412±6, 664±7, and 253±5 km.

The corrected d410 and d660 depths are still strongly correlated with an XCC of 0.69, suggesting that the apparent depths are inadequately corrected, as demonstrated by the significantly shallower corrected depths beneath the WUS relative to the CEUS for both discontinuities (Figure 8). This probably implies that the velocity anomalies in DNA13 are lower than the real values. Indeed, the peak-to-peak upper mantle anomalies in DNA13-Vp (Figure 5b) are only about one third to one half of those in MITP13 (Figure 5a). This difference is mostly due to the use of a high damping factor, which is intended to prevent overinterpretation of small features.

3.3.2. Correction Using MITP13

In an olivine-dominated phase-transition system, which probably prevails in the study area as a whole, both cold and warm regions as well as the presence of water in both the top and bottom of the MTZ lead to an anticorrelation between the depths of d410 and d660. Consequently, the reliability of the corrected results can be evaluated from the XCC between the corrected d410 and d660 depths. A negative or near-zero XCC is expected in the ideal case, while incorrect velocity models lead to large positive XCCs. Guided by this principle, we next perform velocity corrections using MITP13. The original MITP13 model has a vertical interval of 22.59 km. It is resampled into 10 km using the Akima spline method [*Wessel and Smith*, 1998] to facilitate velocity corrections. For a given circle, the *S* wave velocity anomaly, $d\ln(V_S)$, is calculated using the *P* wave anomaly and an optimal γ value, which is defined as $\gamma = d\ln(V_S)/d\ln(V_P)$.

We search for the optimal γ separately for the WUS and CEUS that gives the minimum XCC between the corrected d410 and d660 depths. The searching range for γ is 1.0–3.0, with a step of 0.05. For a candidate γ, d410 and d660 depths for each of the circles are corrected using $V_P(z)$ in MITP13 and $V_S(z)$ computed using $V_P(z)$ and the γ value. The corrected d410 and d660 depths are then used to compute an XCC value. The resulting XCC versus γ curves (Figure 9) show an optimal γ value of 2.15 and 1.70 for the WUS and CEUS, respectively, and the corresponding minimum XCC is 0.30 and 0.57. The difference in the minimum XCC may indicate greater spatial variability of the actual γ value in the CEUS than that in the WUS. Another cause could be a less accurately determined MITP13 for the CEUS due to the fact that a large portion of the area was not sampled by the USArray when the tomographic inversion was conducted [*Burdick et al.*, 2014].

After the corrections using the optimal γ values, the XCC between the corrected depths of d410 and d660 reduces from 0.84 to 0.41 and that between the corrected d410 depths and V_P anomalies changes from −0.81 to −0.31 (Figures 6 and 10). In addition, the mean depth for the entire study area is 417±7 km for d410 and 668±6 km for d660, and the MTZ thickness is 250±7 km. These values are 421±7, 669±6, and 247±8 km

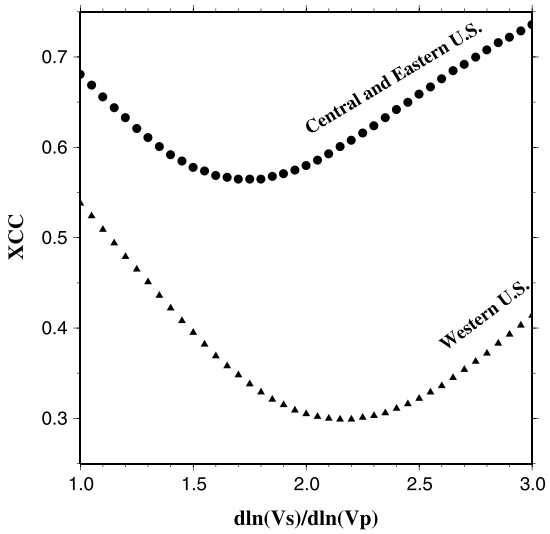

Figure 9. Cross-correlation coefficients between corrected d410 and d660 depths plotted against $d\ln(V_S)/d\ln(V_P)$ (or γ) values used for making depth corrections. Circles are for the CEUS, and triangles are for the WUS. The optimal $d\ln(V_S)/d\ln(V_P)$ value corresponding to the minimum XCC is 2.15 for the WUS and 1.70 for the CEUS.

for the WUS and 415±5, 667±6, and 252±5 km for the CEUS (Figure 11). While the MTZ thickness is still statistically the same between the two areas, the corrected d410 depth between the two areas reduces from 15 km before the corrections to 6 km after the corrections. A similar amount of the reduction is observed for d660. Note that in spite of the differences in the original and corrected (using DNA13 and MITP13) depths, the original and corrected mean MTZ thickness almost remains the same and is within 3 km from the normal value of 250 km for both the WUS and CEUS.

We acknowledge that the above procedure produces reliable results only if γ is fairly uniform over a large area. In addition, the procedure assumes that temperature or water-content anomalies at the top and the bottom of the MTZ have the same sign so that the topography on d410 and d660 tends to anticorrelate. In reality, local variations in γ can produce spurious topography of the discontinuities and artificial lateral variations in MTZ thickness. Attempts have been made to search for the optimal γ value in smaller areas, so that a high-resolution spatial distribution of γ could be obtained. Unfortunately, probably due to the fact that a large number of measurements are needed in order to obtain reliable XCC results, for many of the areas there is no clear minimum on the XCC versus γ curve. Consequently, in the above we assumed a constant γ of 2.15 for the WUS and 1.70 for the CEUS. This assumption certainly leads to inaccurate corrected depths; however, given the similarities in tectonic characteristics and upper mantle velocity structures (Figure 5) within each of the two areas, the biases are expected to be not too significant to invalidate the major conclusions. Additionally, there is a high similarity among the original and corrected MTZ thicknesses (Figures 4c, 8c, and 11c). For instance, the corrected MTZ thicknesses using DNA13 and MITP13 have an almost unity XCC of 0.96 (for the area west of 72°W). This similarity suggests that the use of a constant γ for a large region is appropriate for most of the study area.

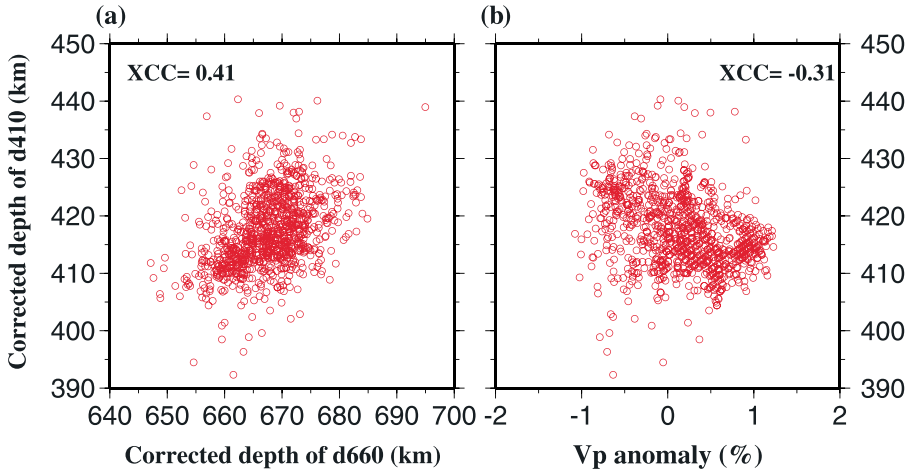

Figure 10. (a) Corrected (using MITP13) d410 depths versus corrected d660 depths. (b) Corrected d410 depths plotted against average *P* wave velocity anomalies in the 0–406 km depth range in the MITP13 model. Note the significant reductions of the absolute value of the XCC relative to the uncorrected situation (Figure 6).

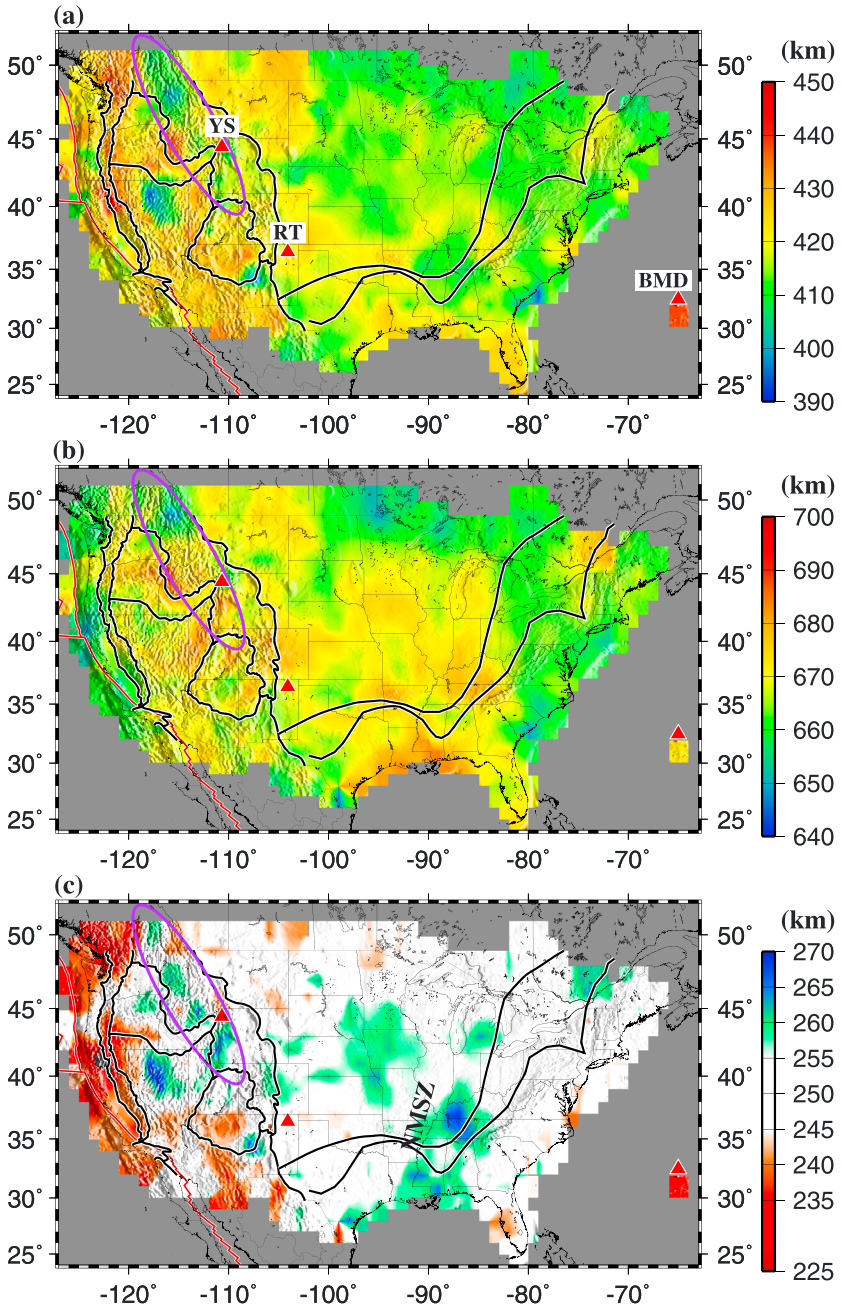

Figure 11. Same as Figure 4 but for corrected d410 and d660 depths using MITP13 and the optimal $d\ln(V_S)/d\ln(V_P)$ values shown in Figure 9. The triangles represent proposed hot spots, and the ellipse outlines the portion of the Juan de Fuca slab in the MTZ. NMSZ: New Madrid Seismic Zone.

4. Discussion

A rich set of features can be observed from the resulting MTZ thickness and discontinuity depth distributions (Figures 4, 8, and 11), as well as from the depth series cross sections (Figures 3 and S1). In this section we briefly discuss some of the first-order features in terms of their depth extent. More detailed discussions of the features are out of the scope of the current paper and are subjects of future regional-scale studies.

4.1. Comparison Between the WUS and CEUS

Under the assumption that the velocity corrections using MITP13 are accurate, the ~6 km depression of d410 relative to the normal value of 410 km suggests that beneath the WUS, the upper MTZ is about 70°K

hotter than normal. The similar amount of depression of d660 suggests that the lower MTZ is about 100°K colder than normal beneath the WUS. Another mechanism that can lead to depressions of both discontinuities is the existence of water [e.g., *Cao and Levander*, 2010] in the lower part of a hot MTZ. Alternatively, the similar amount of depressions of both discontinuities may simply be the results of inadequate velocity corrections, either due to inaccuracies in the velocity models or due to the assumption of a constant γ for the WUS and CEUS or a combination of the two.

The MTZ thickness is within 3 km from the normal value of 250 km for both the WUS and CEUS and for both the original and velocity-corrected depths. This observation suggests that on average, the MTZ beneath the two areas, which have contrasting surface tectonic expressions, are indistinguishable and are similar to the global average in terms of temperature and perhaps also composition. In contrast, the upper mantle structure and physical states are significantly different between the two areas, as evidenced by the contrasting velocity anomalies (Figure 5) and the different optimal γ values (Figure 9).

Mineral physical and numerical modeling experiments suggest that temperature variations in the mantle lead to variations in γ in the range of 1.2–2.0, and partial melting may result in a value of as high as 2.4 [*Kern and Richter*, 1981; *Schmeling*, 1985; *Anderson et al.*, 1992; *Goes et al.*, 2000]. Therefore, a γ value of 1.70 observed for the CEUS suggests a subsolidus upper mantle, while a value of 2.15 for the WUS indicates the existence of wide-spreading partial melting in the upper mantle beneath the area, a conclusion that is consistent with previous studies [e.g., *Schmandt and Humphreys*, 2010].

4.2. Depth Extent of the Proposed Yellowstone Mantle Plume

The existence of a deep (i.e., lower mantle) plume beneath Yellowstone (which is centered at 110.67°W and 44.43°N) has been an issue of heated debates since the 1970s [*Carlson and Hart*, 1987; *Leeman et al.*, 2009; *Smith et al.*, 2009; *Faccenna et al.*, 2010; *Fouch*, 2012]. While virtually all of the previous seismic tomography studies revealed a low-velocity upper mantle beneath Yellowstone, the depth extent of the low-velocity feature remains controversial [*Montelli et al.*, 2006; *Humphreys et al.*, 2000; *Smith et al.*, 2009; *James et al.*, 2011]. Similarly, contrasting conclusions regarding the topography of d410 and d660 have been put forward. Some previous studies [e.g., *Fee and Dueker*, 2004; *Schmandt et al.*, 2012; *Tauzin et al.*, 2013] suggested the existence of a thinned MTZ. For instance, *Schmandt et al.* [2012] revealed a normal d410 depth but a d660 that is uplifted by up to 18 km in an approximately $R = 1.5°$ area centered at about 75 km NE of Yellowstone. The studies of *Waite et al.* [2006] and *Smith et al.* [2009] revealed a tilting plume stem that enters the MTZ at about 150 km northwest of the Yellowstone Caldera. Other studies [e.g., *Christiansen et al.*, 2002; *Deuss*, 2007; *Cao and Levander*, 2010; *Gao and Liu*, 2013], however, were unable to trace the upper mantle anomaly to the top of the MTZ.

No obvious undulations of either discontinuity beneath Yellowstone (feature II in Figure 3b) are observed along the 44°N profile (Figures 3b and S1g), which traverses Yellowstone. Along this profile, the uncorrected depth for d410 is 428 km, and that for d660 is 681 km, leading to an MTZ thickness of 253 km. Similar values are observed for the neighboring profiles (Figures S1f and S1h). The corresponding values corrected using DNA13 are 415, 667, and 252 km, and those corrected using MITP13 are 418, 670, and 252 km. The MTZ thickness is consistent with the result of 253.9 km of *Deuss* [2007] obtained using SS precursors. The reduction in the stacking amplitude of d410 and perhaps d660 in the vicinity of the Yellowstone Caldera is probably due to the anomalously high attenuation associated with the high temperature and partial melting in the upper mantle, as evidenced by the low seismic velocities (Figure 5). The normal MTZ thickness suggests that at the present time, the high temperature anomalies beneath Yellowstone are limited in the upper mantle. There is, however, an area of slight MTZ thinning to the north of the Yellowstone Caldera, although the amount and the area of the thinning are significantly smaller than those observed beneath the Pacific Cost Ranges and the southern Basin and Range Province (Figure 11c).

The key to reveal the true depth of the MTZ discontinuities beneath Yellowstone (and elsewhere) is the accuracy of *P* and *S* wave velocity models needed for making reliable velocity corrections. The accuracy of velocity anomalies in the MTZ is especially critical, because an erroneously introduced low-velocity zone (LVZ) in the MTZ will result in an artificial uplift of d660. The combination of the apparent LVZ and uplifted d660 can be considered as the "perfect" evidence of a hot mantle plume traversing d660 (see Figure 3 in *Mohamed et al.*, 2014 for a quantitative evaluation of this scenario). Conversely, if in reality there is an LVZ in the MTZ, but the LVZ is not included in the velocity models used for making depth corrections, an

erroneously thicker-than-real MTZ will be obtained, leading to the incorrect conclusion that the plume stem does not traverse the MTZ.

4.3. MTZ Beneath Raton and Bermuda

The proposed Raton hot spot [*Morgan and Phipps Morgan*, 2007] has a normal MTZ thickness which is inconsistent with the hypothesis that it is a lower mantle plume. This conclusion is in agreement with the observation that there is a lack of age progression for the volcanic centers along the Jemez volcanic line [*Aldrich*, 1986].

In contrast to the apparently normal MTZ thickness beneath Yellowstone and Raton, the MTZ beneath another proposed hot spot, the Bermuda [*Morgan*, 1983], is thinned by as much as 16 km relative to the normal MTZ thickness of 250 km in the IASP91 model, mostly due to the deepening of d410 (Figures 11 and S1t). This observation confirms the results of *Benoit et al.* [2013], who reported a reduced MTZ thickness of 215 km (which is thinner than the observed 234 km from this study). The 16 km depression of d410 corresponds to a positive temperature anomaly of about 195° in the vicinity of the upper boundary of the MTZ. We emphasize that this conclusion was based on limited (relative to areas on the mainland) amount of data recorded by a single ocean island station. Additional seismological investigations, preferably using data recorded by ocean bottom seismometers, are needed to test the hypothesis that the proposed Bermuda hot spot has a MTZ or lower mantle origin.

4.4. Hot MTZ Beneath the Pacific Coast Ranges and Southern BRP

The thinnest MTZ in the study area is found beneath the Pacific Coast Ranges. The thinning is mostly due to the depression of d410 rather than the uplift of d660 (Figure 11). The magnitude of the depression is about 20–30 km, corresponding to a high temperature anomaly of 240–365°K in the vicinity of d410. Similarly, the MTZ beneath the southern Basin and Range Province and the SW part of the Colorado Plateau is 5–10 km thinner than normal and is also mostly due to the depression of d410 (Figure 11). This observation is not an artifact from imperfect velocity corrections, because the depression of d410 in this area is also observed in the uncorrected results (Figure 4). The spatial distribution and the magnitude of the thinning are in general agreement with those from previous studies [*Cao and Levander*, 2010; *Schmandt et al.*, 2012; *Tauzin et al.*, 2013].

4.5. Location of the Juan de Fuca Slab in the MTZ

Approximately along the Rocky Mountains north of 39°N, the uplift of d410 and the depression of d660 lead to a thickening of the MTZ of up to 15 km (Figure 11). This observation, together with corresponding high-velocity features imaged by seismic tomography (Figures S1a–S1m), confirms that the actively subducting Juan de Fuca slab interacts with the MTZ discontinuities beneath the Rocky Mountains. The location is consistent with the results of *Cao and Levander* [2010] and *Pavlis* [2011]. Beneath this area the stacking amplitudes of the *P*-to-*S* converted phase associated with d410 are among the smallest in the entire study area (Figure 7), mostly due to the combination of a highly attenuating upper mantle and laterally rapid-varying d410 topography.

4.6. Farallon Slab Segments in the Lower MTZ Beneath the Great Plains?

The Great Plains area, which covers the central part of the study area, is characterized by normal d410 depths and a zone of greater-than-normal d660 depths (Figure 11). The shape of this zone is consistent with the high-velocity area in the MTZ found by *Porritt et al.* [2013], who suggested that it represents subducted Farallon slab segments [see *Porritt et al.*, 2013, Figure 8]. The largest depression of d660 is located east of the New Madrid Seismic Zone (Figure 11c). The magnitude of the depression is about 10 km, corresponding to a negative temperature anomaly of about 280°K when a Clapeyron slope of −1.3 MPa/K [*Fei et al.*, 2004] is used. Using the relationship of $dV_P/dT = -0.00048$ km/s/K [*Deal et al.*, 1999], the temperature anomaly corresponds to a V_P anomaly of about 1.5%, which is comparable to the velocity anomalies found by seismic tomography studies [*Burdick et al.*, 2014; *Porritt et al.*, 2013].

In summary, this study provides independent supporting evidence for the existence of the Farallon or Laramide slabs in the MTZ beneath the central United States previously revealed by seismic tomography studies [*Sigloch*, 2011; *Pavlis et al.*, 2012; *Porritt et al.*, 2013].

4.7. Two Circular Areas of Cold MTZ

Beneath the WUS, the two areas with the greatest uplift of d410 are located in the northern Basin and Range Province (Figures 3c and 11c) and the southmost part of the Colorado Plateau (Figure 3d). The former was

investigated using a number of seismological techniques and was proposed to be a lithospheric drip [*West et al.*, 2009] that tilts toward the east and traverses both d410 and d660.

The corrected depth of d410 is 392 km, while that of d660 is 662 km, leading to a 19 km of MTZ thickening (Figure 11). The nearly normal depth of d660 suggests that the drip may not extend to the bottom of the MTZ. Alternatively, the temperature anomalies associated with this cold feature might be too small to cause a detectable depression of d660. This conclusion is consistent with the observation that in the vicinity of the cold area, the stacking amplitude of the *P*-to-*S* converted phase from d410 is weaker than the surrounding areas (Figure 7), probably due to significant tilting of d410. The amplitude of d660, on the other hand, is similar to the surrounding areas.

Another circular area with uplifted d410 and normal d660 is found beneath the southern Colorado Plateau (Figures 11 and 3d). Relative to the one beneath the northern Basin and Range Province, it has a smaller size but a similar amount of d410 uplift and a comparable amount of MTZ thickening of 17 km. Unlike the former, this area is not associated with significant reduction of azimuthal anisotropy as revealed by shear wave splitting measurements [*Liu et al.*, 2014]. In addition, the upper mantle has normal or even slightly negative velocity anomalies (Figure S1q). An alternative explanation for both cold areas is that they represent segments of the Farallon slab [*Pavlis et al.*, 2012]. Obviously, more investigations are needed in order to pinpoint the nature of these interesting features and explore their role in mantle dynamics.

5. Conclusions

Using over 310,000 high-quality receiver functions recorded in the contiguous United States over the past 25+ years, we mapped the topography of the 410 km and 660 km discontinuities using nonplane wave moveout corrections and CCP stacking. The MTZ thickness between the tectonically active western U.S. and the relatively stable central and eastern U.S. is within 3 km from the normal thickness of 250 km, suggesting an overall normal MTZ temperature for both areas and that the contrasts in tectonic activity and physical properties observed on the surface are largely limited in the upper mantle. The upper mantle $d\ln(V_S)/d\ln(V_P)$ value estimated based on the correlation between d410 and d660 depths is 2.15 for the western U.S. and 1.70 for the central and eastern U.S., indicating wide-spreading partial melting in the upper mantle beneath the former. The proposed Yellowstone and Raton hot spots are not associated with a significant depression of d410 or uplift of d660, while a depressed d410 and a normal d660 are observed beneath Bermuda. The Pacific Coast Ranges and Cascade Range are underlain by a significantly depressed d410 and a d660 with normal depth, and the proposed lithospheric drip beneath the northern Basin and Range Province and a circular area beneath the southern Colorado Plateau correspond to an uplifted d410. A zone of uplifted d410 suggests that the Juan de Fuca slab enters the MTZ approximately beneath the Rocky Mountains, while a region of depressed d660 beneath the Great Plains is consistent with the tomographically imaged high-velocity regions in the lower MTZ and uppermost lower mantle, probably reflecting Farallon slab segments subducted over the past 150 million years.

Acknowledgments

Data used in the study were obtained from the IRIS Data Management Center. We thank Rob Porritt for discussions on DNA13 and Gary Pavlis for sending locations of the Farallon slab in digital form. Constructive reviews by Gary Pavlis and an anonymous reviewer significantly improved the manuscript. This study was partially supported by the U.S. National Science Foundation under grant EAR-0952064 and the University of Missouri Research Board.

References

Aldrich, M. J. (1986), Tectonics of the Jemez lineament in the Jemez Mountains and Rio Grande rift, *J. Geophys. Res.*, *91*, 1753–1762, doi:10.1029/JB091iB02p01753.

Ammon, C. J. (1991), The isolation of receiver effects from teleseismic *P*-waveforms, *Bull. Seismol. Soc. Am.*, *81*, 2504–2510.

Anderson, D. L. (2001), Top-down tectonics?, *Science*, *293*, 2016–2018, doi:10.1126/science.1065448.

Anderson, O. L., D. Isaak, and H. Oda (1992), High temperature elastic constant data on minerals relevant to geophysics, *Rev. Geophys.*, *30*, 57–90, doi:10.1029/91RG02810.

Benoit, M. H., M. D. Long, and S. D. King (2013), Anomalously thin transition zone and apparently isotropic upper mantle beneath Bermuda: Evidence for upwelling, *Geochem. Geophys. Geosyst.*, *14*, 4282–4291, doi:10.1002/ggge.20277.

Bina, C. R., and G. Helffrich (1994), Phase transition Clapeyron slopes and transition zone seismic discontinuity topography, *J. Geophys. Res.*, *99*, 15,853–15,860.

Burdick, S., R. D. Van Der Hilst, F. L. Vernon, V. Martynov, T. Cox, J. Eakins, G. H. Karasu, J. Tylell, L. Astiz, and G. L. Pavlis (2014), Model update January 2013: Upper mantle heterogeneity beneath North America from travel-time tomography with global and USArray Transportable Array data, *Seismol. Res. Lett.*, *85*, 77–81, doi:10.1785/0220130098.

Cao, A., and A. Levander (2010), High-resolution transition zone structures of the Gorda slab beneath the western United States: Implication for deep water subduction, *J. Geophys. Res.*, *115*, B07301, doi:10.1029/2009JB006876.

Carlson, R. W., and W. K. Hart (1987), Crustal genesis on the Oregon Plateau, *J. Geophys. Res.*, *92*, 6191–6206, doi:10.1029/JB092iB07p06191.

Christiansen, R. L., G. R. Foulger, and J. R. Evans (2002), Upper mantle origin of the Yellowstone hotspot, *Geol. Soc. Am. Bull.*, *114*, 1245–1256.

Deal, M. M., G. Nolet, and R. D. van der Hilst (1999), Slab temperature and thickness from seismic tomography: 1. Method and application to Tonga, *J. Geophys. Res.*, *104*, 28,789–28,802, doi:10.1029/1999JB900255.

Deuss, A. (2007), Seismic observations of transition-zone discontinuities beneath hotspot locations, Special Papers of the Geological Society of America, *Plates Plumes Planet. Processes*, *430*, 121–136.
Deuss, A., S. A. Redfern, K. Chambers, and J. H. Woodhouse (2006), The nature of the 660-kilometer discontinuity in Earth's mantle from global seismic observations of PP precursors, *Science*, *311*, 198–201.
Dueker, K. G., and A. F. Sheehan (1997), Mantle discontinuity structure from midpoint stacks of converted P to S waves across the Yellowstone hotspot track, *J. Geophys. Res.*, *102*, 8313–8327.
Dziewonski, A. M., and D. L. Anderson (1981), Preliminary reference Earth model, *Phys. Earth Planet. Inter.*, *25*, 297–356.
Faccenna, C., T. W. Becker, S. Lallemand, Y. Lagabrielle, F. Funiciello, and C. Piromallo (2010), Subduction-triggered magmatic pulses: A new class of plumes?, *Earth Planet. Sci. Lett.*, *299*, 54–68, doi:10.1016/j.epsl.2010.08.012.
Fee, D., and K. Dueker (2004), Mantle transition zone topography and structure beneath the Yellowstone hotspot, *Geophys. Res. Lett.*, *31*, L18603, doi:10.1029/2004GL020636.
Fei, Y., J. Van Orman, J. Li, W. Van Westrenen, C. Sanloup, W. Minarik, and K. I. Funakoshi (2004), Experimentally determined postspinel transformation boundary in Mg_2SiO_4 using MgO as an internal pressure standard and its geophysical implications, *J. Geophys. Res.*, *109*, B02305, doi:10.1029/2003JB002562.
Flanagan, M. P., and P. M. Shearer (1998), Global mapping of topography on transition zone velocity discontinuities by stacking *SS* precursors, *J. Geophys. Res.*, *103*, 2673–2692, doi:10.1029/97JB03212.
Fouch, M. J. (2012), The Yellowstone hotspot: Plume or not?, *Geology*, *40*, 479–480, doi:10.1130/focus052012.1.
Gao, S. S., and K. H. Liu (2013), Imaging mantle discontinuities using multiply-reflected P-to-S conversions, *Earth Planet. Sci. Lett.*, *402*, 99–106, doi:10.1016/j.epsl.2013.08.025.
Goes, S., R. Govers, and P. Vacher (2000), Shallow mantle temperatures under Europe from P and S wave tomography, *J. Geophys. Res.*, *105*, 11,153–11,169.
Gu, Y., A. M. Dziewonski, and C. B. Agee (1998), Global de-correlation of the topography of transition zone discontinuities, *Earth Planet. Sci. Lett.*, *157*, 57–67.
Hirose, K. (2002), Phase transitions in pyrolitic mantle around 670-km depth: Implications for upwelling of plumes from the lower mantle, *J. Geophys. Res.*, *107*(B4), ECV 3-1–ECV 3-13, doi:10.1029/2001JB000597.
Hoffman, P. F. (1988), United plates of America, the birth of a craton: Early Proterozoic assembly and growth of Laurentia, *Annu. Rev. Earth Planet. Sci.*, *16*, 543–603.
Humphreys, E., K. Dueker, D. Schutt, and R. Smith (2000), Beneath Yellowstone: Evaluating plume and nonplume models using teleseismic images of the upper mantle, *Geol. Soc. Am.*, *10*, 1–7.
James, D. E., M. J. Fouch, R. W. Carlson, and J. B. Roth (2011), Slab fragmentation, edge flow and the origin of the Yellowstone hotspot track, *Earth Planet. Sci. Lett.*, *311*, 124–135, doi:10.1016/j.epsl.2011.09.007.
Katsura, T., A. Ueda, E. Ito, and K.-I. Morooka (2003), Post-Spinel transition in Fe2SiO4, in *Properties of Earth and Planetary Materials at High Pressure and Temperature*, edited by M. H. Manghnani, and T. Yagi, AGU, Washington, D. C., doi:10.1029/GM101p0435.
Kennett, B. L. N., and E. R. Engdahl (1991), Traveltimes for global earthquake location and phase identification, *Geophys. J. Int.*, *105*, 429–465, doi:10.1111/j.1365-246X.1991.tb06724.x.
Kennett, B. L. N., E. R. Engdahl, and R. Buland (1995), Constraints on seismic velocities in the Earth from traveltimes, *Geophys. J. Int.*, *122*, 108–124.
Kern, H., and A. Richter (1981), Temperature derivatives of compressional and shear wave velocities in crustal and mantle rocks at 6 kbar confining pressure, *J. Geophys.*, *49*, 47–56.
Leeman, W. P., D. L. Schutt, and S. S. Hughes (2009), Thermal structure beneath the Snake River Plain: Implications for the Yellowstone hotspot, *J. Volcanol. Geotherm. Res.*, *188*, 57–67, doi:10.1016/j.jvolgeores.2009.01.034.
Litasov, K. D., E. Ohtani, A. Suzuki, and K. Funakoshi (2005), Wet subduction versus cold subduction, *Geophys. Res. Lett.*, *32*, L13312, doi:10.1029/2005GL022921.
Liu, K. H. (2003), Effects of inelasticity on the apparent depth and detectability of seismic discontinuities in the mantle, *Geophys. Res. Lett.*, *30*(9), 1455, doi:10.1029/2002GL015264.
Liu, K. H., S. S. Gao, P. G. Silver, and Y. Zhang (2003), Mantle layering across central South America, *J. Geophys. Res.*, *108*(B11), 2510, doi:10.1029/2002JB002208.
Liu, K. H., and S. S. Gao (2010), Spatial variations of crustal characteristics beneath the Hoggar swell, Algeria, revealed by systematic analyses of receiver functions from a single seismic station, *Geochem. Geophys. Geosyst.*, *11*, Q08011, doi:10.1029/2010GC003091.
Liu, K. H., A. Elsheikh, A. Lemnifi, U. Purevsuren, M. Ray, H. Refayee, B. Yang, Y. Yu, and S. S. Gao (2014), A uniform database of teleseismic shear wave splitting measurements for the western and central United States, *Geochem. Geophys. Geosyst.*, *15*, 2075–2085, doi:10.1002/2014GC005267.
Liu, X., and G. L. Pavlis (2013), Appraising the reliability of converted wavefield imaging: Application to USArray imaging of the 410-km discontinuity, *Geophys. J. Int.*, *192*, 1240–1254, doi:10.1093/gji/ggs088.
Lowry, A. R., N. M. Ribe, and R. B. Smith (2000), Dynamic elevation of the Cordillera, western United States, *J. Geophys. Res.*, *105*, 23,371–23,390.
Mohamed, A. A., S. S. Gao, A. A. Elsheikh, K. H. Liu, Y. Yu, and R. E. Fat-Helbary (2014), Seismic imaging of mantle transition zone discontinuities beneath the northern Red Sea and adjacent areas, *Geophys. J. Int.*, doi:10.1093/gji/ggu284.
Montelli, R., G. Nolet, F. A. Dahlen, and G. Masters (2006), A catalogue of deep mantle plumes: New results from finite frequency tomography, *Geochem. Geophys. Geosyst.*, *7*, Q11007, doi:10.1029/2006GC001248.
Morgan, W. J. (1983), Hotspot tracks and the early rifting of the Atlantic, *Tectonophysics*, *94*, 123–139.
Morgan, W. J., and J. Phipps Morgan (2007), Plate velocities in the hotspot reference frame, *Geol. Soc. Am. Spec. Pap.*, *430*, 65–78, doi:10.1130/2007.2430.
Pavlis, G. L. (2011), Three dimensional wavefield imaging of data from the USArray: New constraints on the geometry of the Farallon slab, *Geosphere*, *7*, 785–801.
Pavlis, G. L., K. Sigloch, S. Burdick, M. J. Fouch, and F. L. Vernon (2012), Unraveling the geometry of the Farallon plate: Synthesis of three-dimensional imaging results from USArray, *Tectonophysics*, *532*, 82–102, doi:10.1016/j.tecto.2012.02.008.
Porritt, R. W., R. M. Allen, and F. F. Pollitz (2013), Seismic imaging east of the Rocky Mountains with USArray, *Earth Plant. Sci. Lett.*, *402*, 16–25, doi:10.1016/j.epsl.2013.10.034.
Ringwood, A. E. (1975), *Composition and Petrology of the Earth's Mantle*, McGraw-Hill, New York.
Schmandt, B., and E. Humphreys (2010), Complex subduction and small-scale convection revealed by body-wave tomography of the western United States mantle, *Earth Planet. Sci. Lett.*, *297*, 435–445, doi:10.1016/j.epsl.2010.06.047.

Schmandt, B., K. Dueker, and E. Humphreys (2012), Hot mantle upwelling across the 660 beneath Yellowstone, *Earth Planet. Sci. Lett.*, *331-332*, 224–236, doi:10.1016/epsl.2012.03.025.

Schmeling, H. (1985), Numerical models on the influence of partial melt on elastic, anelastic, and electrical properties of rocks. Part I: Elasticity and anelasticity, *Phys. Earth Planet. Inter.*, *41*, 34–57, doi:10.1016/0031-9201(85)90100-1.

Shearer, P. M. (1991), Constraints on upper mantle discontinuities from observations of long-period reflected and converted phases, *J. Geophys. Res.*, *96*, 18,147–18,182.

Sigloch, K. (2011), Mantle provinces under North America from multifrequency P wave tomography, *Geochem. Geophys. Geosyst.*, *12*, Q02W08, doi:10.1029/2010GC003421.

Smith, R. B., M. Jordan, B. Steinberger, C. M. Puskas, J. Farrell, G. P. Waite, S. Husen, W. L. Chang, and R. O'Conne (2009), Geodynamics of the Yellowstone hotspot and mantle plume: Seismic and GPS imaging, kinematics, and mantle flow, *J. Volcanol. Geotherm. Res.*, *188*, 26–56, doi:10.1016/j.jvolgeores.2009.08.020.

Smyth, J. R. (1987), b-Mg2SiO4: A potential host for water in the mantle?, *Am. Mineral.*, *72*, 1051–1055.

Smyth, J. R., and D. J. Frost (2002), The effect of water on the 410-km discontinuity: An experimental study, *Geophys. Res. Lett.*, *29*(10), 123-1–123-4, doi:10.1029/2001GL014418.

Tauzin, B., R. D. van der Hilst, G. Wittlinger, and Y. Ricard (2013), Multiple transition zone seismic discontinuities and low velocity layers below western United States, *J. Geophys. Res. Solid Earth*, *118*, 2307–2322, doi:10.1002/jgrb.50182.

Torsvik, T. H., B. Steinberger, M. Gurnis, and C. Gaina (2010), Plate tectonics and net lithosphere rotation over the past 150 My, *Earth Planet. Sci. Lett.*, *291*, 106–112.

Waite, G. P, R. B. Smith, and R. M. Allen (2006), Vp and Vs structure of the Yellowstone hot spot: Evidence for an upper mantle plume, *J. Geophys. Res.*, *111*, B04303, doi:10.1029/2005JB003867.

Wessel, P., and W. H. F. Smith (1998), New, improved version of Generic Mapping Tools released, *Eos Trans. AGU*, *79*(47), 579–579, doi:10.1029/98EO00426.

West, J. D., M. J. Fouch, J. B. Roth, and L. T. Elkins-Tanton (2009), Vertical mantle flow associated with a lithospheric drip beneath the Great Basin, *Nat. Geosci.*, *2*, 439–444, doi:10.1038/ngeo526.